Distinct roles of microtubules and actin filaments in defining dendritic architecture

Sumit Nanda[1], Shatabdi Bhattacharjee[2], Daniel N. Cox[2], Giorgio A. Ascoli[1,3]*

1. Center for Neural Informatics, Structures, & Plasticity and Neuroscience Program, Krasnow Institute for Advanced Study, George Mason University, Fairfax, VA, USA

2. Neuroscience Institute, Georgia State University, Atlanta, GA, USA

3. Bioengineering Department, Volgenau School of Engineering, George Mason University, Fairfax, VA, USA

*Correspondence: ascoli@gmu.edu

Abstract

Neuronal morphology underlies circuit connectivity and signal integration, thus profoundly affecting nervous system function. Although microtubules and F-actin have long been recognized as key determinants of dendritic morphology, their precise and distinct roles are yet to be fully elucidated. The lack of arbor-wide cytoskeletal information registered with neuromorphological measurements has so far limited direct observations of the interrelations between microtubules, F-actin and arbor architecture. Here we pair live confocal imaging of fluorescently labeled dendritic arborization (da) neurons in the fruit fly larva with our recently developed multi-signal neural tracing technique. We discovered that dendritic arbor length is highly dependent on local microtubule quantity, whereas local F-actin enrichment is associated with dendritic branching. Earlier computer simulations used quantifiable morphological features both as model parameters (*e.g.* branch thickness) and emergent properties (*e.g.* tree asymmetry). Multi-signal reconstructions allowed us to computationally simulate arbor structure solely constrained by experimentally measured, local subcellular distributions of microtubules and F-actin. The generative model yielded synthetic trees with morphological and molecular patterns statistically indistinguishable from those of real da neurons, demonstrating that these two investigated cytoskeletal components are sufficient to define dendritic architecture. The analysis and modeling outcomes hold true for the simplest (Class I) and the most complex (Class IV) da neuron subclasses. Moreover, local increases in the quantity of stable microtubules in Class IV neurons via Formin3 overexpression further strengthens the correlation between local microtubule quantity and dendritic arbor length as predicted by the model and reproduced in simulations.

SUPPORT: NIH R01 NS39600 and NS086082 and BICCN U01 MH114829.

Significance

Microtubules and F-actin are fundamental molecular factors in neuronal arbor architectural development. However, the elucidation of their exact roles in defining dendritic architecture has been hindered by the lack of arbor-wide cytoskeletal information in existing morphological data. Our recently developed enhanced digital tracing methodology allows the systematic quantification of subcellular protein distributions with overall morphology. These multi-signal reconstructions and the novel analyses reported in this study demonstrate two striking double-dissociations in cytoskeletal behavior: local microtubule is the best predictor of arbor length, while local enrichment in F-actin is strongly associated with branching. A computational model of arbor generation purely driven by local microtubule and F-actin quantities fully

reproduces tree topology and dendritic cytoskeletal distributions. Moreover, these findings are robust across cell types and genetic alteration.

Introduction

Nervous systems comprise of numerous neuronal subtypes, each with its own axonal-dendritic morphology and field of innervation. The specification and dynamic modification of subtype specific dendritic architecture not only dictate how distinct neuron subtypes form functional connections with other neurons, but also directly influences subtype-specific computational properties (1). The broad significance of dendritic form in neural function is further underscored by the wide spectrum of neurological and neurocognitive disorders that have been linked to disruptions in these processes (2). A vital challenge in understanding neuronal architecture is to elucidate how dendritic branches are regulated to elongate, bifurcate and terminate, leading to their unique tree geometry, and how these regulatory rules vary to yield the striking observed diversity in structure, function and connectivity (3). *Drosophila* larval sensory dendritic arborization (da) neurons has proven an exceptionally powerful model for investigating these questions, revealing mechanistic underpinnings of numerous structural dynamics including tilling, remodeling, outgrowth and subtype-specific branching (4, 5).

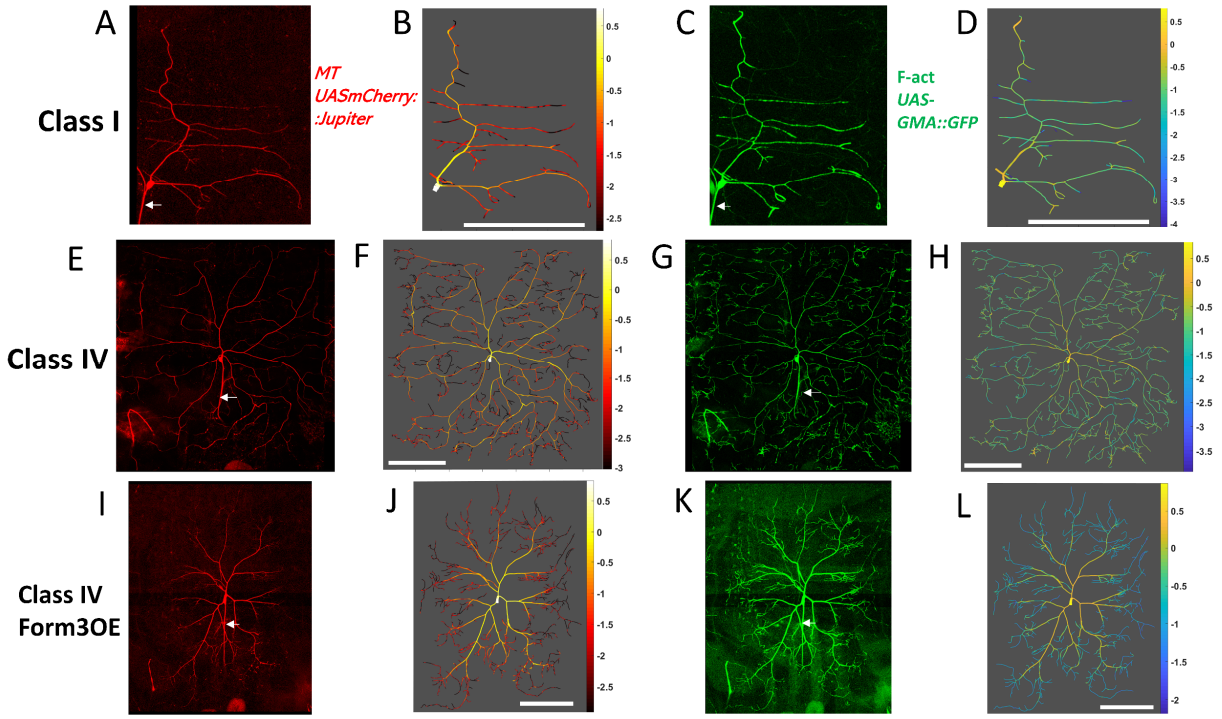

Fig. 1 Confocal images and multi-signal reconstructions of Class I wild type (A, B, C, D), Class IV wild type (E, F, G, H) and Class IV mutant Form3OE (I, J, K, L). Microtubule (A, E, I) and F-actin (C, G, K) signals from confocal image stacks are traced together to produce multi-signal ESWC files, allowing the arbor-wide quantification and graphic rendering of microtubule (B, F, J) and F-actin (D, H, L) intensities (heatmaps represent the log of cytoskeletal quantity). Axons (identified with arrowheads in A, C, E, G, I, K), only partially visible, are not traced and analyzed in this study.

A combination of intrinsic genetic programming, extrinsic cues, electrophysiological activity and proximity to other cells (neuronal and non-neuronal) sculpt mature dendritic shape and maintain arbor stability as well as plasticity (3). Each of these regulatory processes has been demonstrated to impact dendritic architecture by ultimately converging on the cytoskeleton. Furthermore, the acquisition, maintenance, and modulation of diverse dendritic morphologies is largely mediated by organization and dynamics of F-actin and microtubule cytoskeletal components that provide the underlying scaffold and fiber tracks for intracellular trafficking critical to arbor development (2, 6–8). Numerous studies have demonstrated that diverse dendritic morphologies emerge via complex growth mechanisms modulated by intrinsic signaling involving combinatorial transcription factor (TF) regulatory codes that contribute to both neuronal subtype identity and morphological diversity (2, 9-18). These TF-mediated programs converge on a diverse set of cellular pathways to drive dendritic arbor diversity, many of which ultimately impact cytoskeletal architecture as a terminal mediator of arbor shape (2, 12, 19–24).

Neuronal microtubules form a quasi-continuous core within the dendritic tree (25). Microtubules result from the polymerization of α- and β-tubulin heterodimers on a structural template of γ-tubulin. The polarized protofilaments are then laterally arranged into a hollow configuration. Microtubules exhibit dynamic instability, *i.e.* an instant alteration between tubulin assembly and disassembly, allowing dendritic branches to elongate or retract (26). This switching can be intrinsically controlled by GTP/GDP binding to the heterodimers, where the GTP-tubulin lattice promotes polymerization and GDP-tubulin lattice promotes disassembly (27). Unlike axons, whose microtubule rapidly polymerizing ("plus") ends are uniformly oriented in the anterograde direction (28), dendrites have mixed microtubule polarity, and microtubules remain significantly dynamic in mature dendritic trees. Polymerizing microtubules exist in both proximal and distal dendrites, with a dominance of retrograde polymerization in proximal and anterograde polymerization in the distal (nascent) branches. Growing neurons without microtubule organizing centers regulate dendritic microtubule polymerization locally by molecules such as Augmin (29).

F-actin is also a polarized structure, consisting of ATP-bound globular actin primarily polymerizing at the barbed end (6). All motile cells, including neurons, ubiquitously employ F-actin polymerization to drive plasma membrane protrusion. F-actin polymerization is rate-controlled by nucleators such as Arp2/3 complex, which binds to monomeric actin to facilitate polymerization (30, 31) and enables F-actin polymer branching (32), and the formin family, which acts downstream of Rho-GTPases to nucleate unbranched F-actin (33). In addition to their recognized role in actin nucleation and polymerization (33, 34), formins have been also implicated in microtubule stabilization through acetylation of F-hand domains (35). A single molecule, Formin3, was shown to simultaneously regulate the stability and organization of the microtubule and F-actin cytoskeletons, thereby impacting dendritic architecture (24). Moreover, inwards actin waves facilitated by ADF/Cofilin allow microtubules to protrude, stabilizing initial branch growth (36). Recent fluorescence nanoscopic observations also revealed a periodic, ring-like, membrane-attached actin-spectrin scaffold mostly compartmentalizing axonal membrane, but also found in dendrites (37).

Although numerous upstream regulatory pathways have been discovered for microtubules and F-actin, their distinct roles in defining overall dendritic structure are still actively debated. Anterograde microtubule polymerization facilitated by F-actin destabilization allows microtubules to invade filipodia leading to the formation of new branches (38). It has also been shown, however, that microtubule stabilization, rather than polymerization, yields greater branching complexity in newly formed dendrites, while retrograde microtubule polymerization away from bifurcations and terminals restricts overall branching (39). Yet, contrary evidence suggests that microtubule stabilization reduces branch outgrowth in developing arbors (40). Even microtubule "minus" ends, supposedly the stable polymer sides, may display continued polymerization, leading to minus-end out microtubule orientation (41). Growing neurite

tips are often rich in F-actin bundles and actin polymerization drives neurite outgrowth even in the presence of F-actin polymerizing inhibitors, while neurite tips lacking actin do not elongate (42). However, opposing experiments indicate that actin waves at growth cones do not initiate elongation and rather neurite outgrowth occurs without F-actin at neurite tips (43). Actin polymerization is also involved in dendritic branch retraction (44) and retrograde actin flow has been implicated in branch extension (36). Possibly stabilizing actin blobs are also found at branch points (45) and nucleation events have been involved in this punctate expression of F-actin (31). Since the local densities of microtubules and F-actin have never been quantified arbor-wide in large numbers of neurons, the multifarious relation between arbor architecture and cytoskeletal composition remains incompletely understood.

Here we deploy the newly developed multi-modal confocal image stack tracing of multi-fluorescent neurons (46) to reconstruct a representative sample of da morphologies containing arbor-wide local quantifications of microtubule and F-actin concentrations. We then devise novel analyses of these enhanced data uncovering a doubly dissociated effect of microtubules and F-actin on dendritic architecture: local microtubule quantity predicts downstream dendritic length and thereby overall arbor size; conversely, tree complexity is associated with changes in local F-actin quantity, as bifurcating regions are enriched in F-actin. We then show that local cytoskeletal composition is sufficient in constraining complete arbor morphology by designing a generative model that computationally simulates tree structure purely based on local microtubule and local F-actin concentrations measured from real neurons. The analytical observations as well as computer simulation results remain robust across functionally distinct da neuron subclasses and genetic alteration.

Results

Class I and Class IV neurons represent the two extremes in da neuron morphology with respect to arbor size and complexity (14). Class I neurons exhibit the simplest arbors and are the smallest of da neuron subclasses (Fig. 1 A, B, C, D). Conversely, Class IV neurons are space-filling and constitute the most complex and largest da neurons (Fig. 1 E, F, G, H). Here we focused on the Class I ddaE neuron subtype and Class IV ddaC subtype. Moreover, we considered genetic perturbation of cytoskeletal regulation by examining Class IV (ddaC) neurons overexpressing Formin3 (Form3OE), which also differs significantly from the corresponding wild type in both size and complexity (Fig. 1 I, J, K, L). Formin3 overexpression was selected for genetic perturbation based on prior analyses (24) demonstrating a molecular role in differentially regulating dendritic F-actin and microtubule cytoskeletal organization. All three neuron groups were subjected to live, *in vivo* imaging using genetically-encoded, multi-fluorescent transgenic reporter strains to visualize F-actin and microtubule distributions (11). Cytoskeletal organization in control or mutant genetic backgrounds was assessed by using Class I- or Class IV-specific GAL4 to label respectively stable microtubules via the mCherry-tagged microtubule associated protein Jupiter (Fig 1 A, E, I) and F-actin by a GFP-tagged Moesin actin binding domain (Fig. 1 C, G, K). Basic morphological reconstructions of these images consisted of vectorized tree structures composed of numerous, uniformly sampled, connected compartments. Enhanced multi-signal reconstructions were then created from the image stacks starting from the basic reconstruction templates by annotating microtubule (Fig. 1 B, F, J) and F-actin (Fig. 1 D, H, L) intensities in every compartment. Microtubule intensities displayed a similar tapering pattern in all three neuron groups (Fig. 1 B, F, J), generally decreasing with path distance from soma and centrifugal branch order. Conversely, F-actin intensities were more heterogenous without a discernable tapering tendency (Fig. 1 D, H, L).

Morphometric and cytoskeletal differentiation among neuron classes

As expected, quantitative morphometry demonstrated substantial differences among the three neuronal groups in overall size and morphology (Fig. 2 A). Class IV wild type (WT) neurons were clearly the largest in total dendritic length (19,305 ± 1510 µm, N=10) and had the largest spanning field (height 727± 63 µm,

width 593± 32 µm). Genetically altered Class IV Form3OE neurons were smaller (total length 12,591 ± 985 µm, height 627± 44 µm, width 545± 32 µm, N=9), and Class I neurons were by far the smallest in length and spanning field (1680 ± 166 µm, height 260± 21 µm, width 221± 21 µm, N=19). Class IV WT neurons also had the most complex dendritic arbors as measured by the number of branch terminals (683 ± 44.7), followed by Class IV Form3OE (365 ± 29.9) and the least complex Class I (26 ± 4.8). Correspondingly, the maximum Strahler orders for the three groups were 7, 6 and 4, respectively (Fig. 2 D). These results were consistent with previous analyses of da neurons (47, 48).

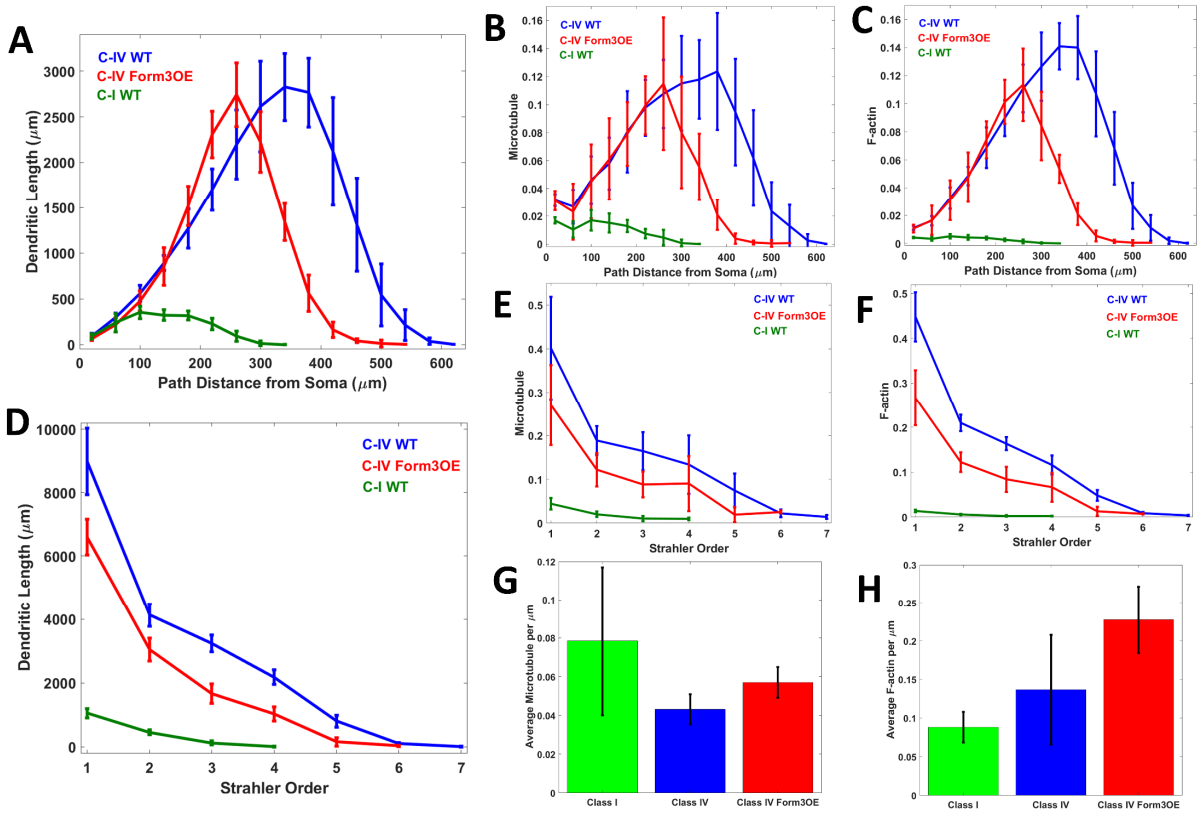

Fig. 2 Morphological and cytoskeletal analysis of three groups of da neurons from the fruit fly larva. Distributions of dendritic length (A, D), microtubule (B, E) and F-actin (C, F) are examined as functions of path distance from soma (A, B, C) and Strahler order (D, E, F) for Class I (green), Class IV (blue) and mutant Class IV (red) neurons. In panels B, C, E, and F the Y axes was scaled so as to obtain unitary area under the curve for Class IV (blue lines). Average microtubule (G) and F-actin (H) quantities are also reported per unit of length. Error bars indicate standard deviation.

The morphological patterns were also reflected in overall intensity distributions for both microtubules (Fig. 2 B, E) and F-actin (Fig. 2 C, F). Notably, on average, Class I had higher microtubule and lower F-actin signal levels (per unit length) compared to Class IV WT and Class IV Form3OE, while Form3OE increased the average local quantities of both microtubule and F-actin in Class IV neurons (Fig. 2 G, H).

Interestingly, the local quantities of microtubules and F-actin paralleled each other in the dendrites near the soma, but not farther out in the dendritic trees. Specifically, in the 20% most proximal dendrites, microtubules and F-actin intensities were highly correlated (Pearson R coefficients: 0.98 for Class I, 0.88 for Class IV and 0.89 for Class IV Form3OE), whereas the 20% most distal locations displayed drastically

reduced correlation (R= 0.46, 0.32 and 0.68 respectively for Class I, Class IV and Class IV Form3OE) (SI Appendix, Table S3).

Tree asymmetry can be quantified as the normalized average over all bifurcations of the difference between the number of terminals (topological asymmetry) or the downstream arbor lengths (length asymmetry) stemming from each of the two children of a branch point. This metric ranges between 0 for a perfectly symmetric tree and 1 for a fully asymmetric tree (49), and can often discriminate among neuron types or even between dendritic arbors within the same neurons, as in the apical and basal trees of pyramidal cells (50). An alternative measure of dendritic asymmetry, caulescence, captures the degree to which a neuron has a main dendritic path or trunk (51) and weighs the imbalance of each bifurcation by the size of its sub-tree, thus emphasizing branches closer to the soma (see Methods for mathematical definition of asymmetry and caulescence). While tree asymmetry did not vary greatly among the three groups of neurons considered here, there were substantial differences in tree caulescence. Class I neurons displayed the clearest main path as reflected by their topological caulescence (0.579 ± 0.091) and even more by length caulescence (0.631 ± 0.107). Class IV dendrites grow out in all directions, and hence did not show an evident main path (topological caulescence: 0.470 ± 0.080, length caulescence: 0.450 ± 0.067). Length and topological caulescence are significantly different between Class I and Class IV WT ($p = 0.00005$ and $p = 0.0036$), as well as between Class I and Class IV Form3OE ($p = 0.0018$ and $p = 0.01$) (SI Appendix, Table S1).

Table 1 Pearson correlation coefficients of arbor length against morphological and cytoskeletal parameters at the resolution of single (2 µm long) compartments. Microtubule quantity is the best predictor of arbor length for all analyzed cell types.

Cell Type	MT quantity	F-act quantity	MT + F-act quantity	Path distance from soma	Branch order	Diameter
Class I	**0.67**	0.55	0.62	-0.47	-0.33	0.64
Class IV	**0.79**	0.43	0.63	-0.45	-0.42	0.49
Class IV Form3OE	**0.88**	0.76	0.82	-0.47	-0.39	0.61

Local microtubule quantity is the best predictor of arbor length

Total arbor length is a strongly discriminant descriptor of dendritic architecture and quantifies tree size by accounting for both overall span and branching complexity (51). Arbor length can be measured not only at the soma, where it captures the total dendritic elongation summed over the whole neuron, but also at any dendritic position considered as the root of the downstream sub-tree (SI Appendix, Fig. S1). Sub-tree arbor length is known to correlate with several geometric characteristics measured at the local root, including path distance from the soma, centrifugal branch order and branch thickness (48, 50). Therefore, these parameters have long been considered numerical proxies of underlying molecular processes that actually shape dendritic architecture (52, 53). The neuron-wide measurement of local microtubule and F-actin quantities allowed us for the first time to directly test how the two major

cytoskeletal mediators of dendritic growth compare with local geometric parameters in predicting downstream sub-tree length across the entire dendritic arbor. Path distance from the soma, centrifugal branch order, branch thickness and downstream arbor length were calculated at every dendritic location in all neurons.

Among all geometric and molecular parameters, microtubule quantity was the best local predictor of arbor length (Table 1). Microtubule quantity captured most arbor length variance in Class IV Form3OE (77.4%) followed by Class IV WT (62.4%) and then Class I (44.9%). Higher quantities of microtubules correlated with greater arbor length and, when microtubule ran out, dendritic branches tended to terminate (SI Appendix, Fig. S1). Correspondingly, the correlation between microtubule quantity and arbor length was also considerably reduced in terminal branches (Table S3), where it only accounted for negligible amounts of variance (6.7% for Class I, 2.6% for Class IV and 0.04% for Class IV Form3OE). This is also consistent with the known greater dynamic plasticity of terminal branches, which can continuously elongate or retract in mature arbors. Interestingly, microtubule quantity alone had a higher correlation with arbor length than when combined with F-actin quantity (Table 1). Among geometric parameters, branch diameter had the highest correlations with both microtubule quantity and arbor length (Table 1). Remarkably, these findings directly confirm early theoretical claims (52).

Bifurcations are strongly associated with local F-actin enrichment

Relative to microtubules, F-actin was distributed more heterogeneously in all three neuron groups and displayed a lower correlation with arbor length (Fig. 1, 2, Table 1). Instead we observed definitive patterns in the relative change of F-actin quantity between adjacent locations. Specifically, a systematic punctate expression of F-actin was qualitatively apparent at dendritic bifurcations (Fig. 3). To quantify this phenomenon, we computed the difference in F-actin signal at every dendritic compartment relative to its parent compartment (ΔF). We then separated all compartments based on their topological behaviors: elongations, bifurcations and terminations. We found that most bifurcating compartments (74% in Class I, 68% in Class IV, and 60% in Class IV Form3OE) showed F-actin enrichment, *i.e.* an increase in F-actin relative to their parent compartments. The cumulative ΔF frequency was significantly right-shifted for bifurcations relative to elongations and terminations in all three neuron groups (Fig. 3). The median ΔF for bifurcations were 0.11, 0.14, and 0.09 in Class I, Class IV, and Class IV Form3OE neurons, respectively. The corresponding median ΔF for elongations were -0.24, -0.044, -0.032, respectively, indicating a tendency of F-actin quantity to decrease along non-bifurcating branches. Only 24% of Class I, 26% of Class IV and 32% of Class IV Form3OE bifurcations displayed a ΔF value lower than the respective elongation medians. This analysis extends and quantifies previous observations of F-actin blobs at branch points (45).

Distinct effects of microtubules and F-actin on dendritic growth and branching

Our quantitative analysis suggests a stark double dissociation between the two major mechanisms to establish dendritic architecture, namely branch elongation and bifurcation, and distinct cytoskeletal determinants, respectively microtubule quantity and F-actin enrichment. Correspondingly, an in-depth inspection of separate topological events (occurrence of terminating, elongating, or bifurcating dendritic branches) as a combined function of local microtubule quantity and relative F-actin change (SI Appendix, Fig. S2 A, B, C) revealed almost entirely complementary cytoskeletal compositions underlying bifurcations (F-actin enrichment independent of microtubule quantity) and terminations (strong decline or absence of microtubules). Only in Form3OE Class IV neurons did elongation-rich and termination-rich regions partially overlap (Fig. S2 C). We also found converging evidence at the dendritic branch level. Class I neurons had a relatively high ratio of microtubule to F-actin quantities (0.89 ± 0.32) and displayed greater average branch length (33.57 ± 5.11 µm), *i.e.* a reduced number of bifurcations relative to total elongation. Class IV neurons (both WT and Form3OE), on the contrary, had shorter branches on average (WT: 14.2 ± 1.0 µm, Form3OE: 17.3 ± 0.7 µm) and lower microtubule to F-actin ratios (WT: 0.38 ± 0.14, Form3OE: 0.25 ±

0.04) (Table S4). In other words, the ratio between arbor size and complexity paralleled the ratio between microtubule and F-actin quantities. Increase in the proportion of arbor lacking detectable microtubule across neuronal groups led to a decrease in average branch length (R = -0.79, p <0.001) (Fig. S3).

Taken together, these interactions may provide a complete description of two fundamental aspects of dendritic arbor topology: size (total length) and complexity (number of branches). Considering this evidence, we proceeded to test whether local microtubules and F-actin measurements could be sufficient to fully reproduce the arbor-wide morphological and cytoskeletal properties for all three neuron groups.

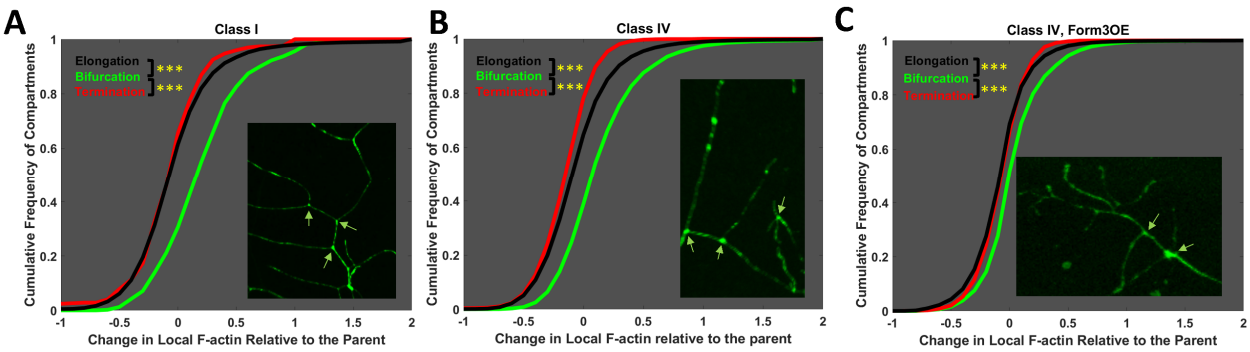

Fig. 3 Cumulative frequency of the fold change in local F-actin concentration relative to the parent compartment for bifurcating (green), elongating (black) and terminating (red) compartments. A value of 0 indicates unchanged F-actin concentration; a value of -1 indicates complete F-actin disappearance (100% decrease relative to parent compartment); and a value of +1 indicates doubling F-actin concentration (100% increase relative to parent compartment). Class I (A), Class IV (B) and mutant Class IV Form3OE (C) distributions are shown separately. In all three cases, the bifurcating line is clearly right-shifted relative to the terminating and elongating lines. The arrowheads in the inset confocal images point to representative branch points. Triple asterisks indicate significantly different comparisons with p<0.001, Bonferroni-corrected 1-tail t-test.

Computational model of arbor generation based on local microtubule and F-actin

Previous studies have shown that neural arbors of various cell types (53, 54), including da neuron arbors (49), can be simulated by computational models constrained by local geometry (path distance, branch order and branch thickness). Our analysis indicated that local cytoskeletal components had greater influence over arbor length and branching probability than previously used geometric parameters. To test the sufficiency of local microtubule and F-actin quantities in reproducing overall tree architecture, we designed a computational model of dendritic morphology purely driven by local quantities of microtubules and F-actin measured from the reconstructed dendritic trees (Fig. 4). The model consisted of two stochastic processes iterated over all generated compartments starting from the dendritic roots stemming from the soma: sampling of topological behavior and sampling of cytoskeletal composition. Thus, in these simulations, local microtubule and F-actin quantities determined not only the branching behavior in that dendritic location, but also the cytoskeletal composition of the child compartment(s). The first stochastic process sampled one of three possible topological events (elongation, bifurcation and termination) from the corresponding cytoskeletal data grid (Fig. 4A). Sampling an elongation event added one child compartment; sampling a bifurcation event added two child compartments; sampling a termination added no compartment and closed the open compartment. The second process, determining the cytoskeletal composition in the child compartments, was further subdivided into two sampling grids for the elongation (Fig. 4B) and bifurcation data (Fig. 4C). The elongation grid contained the cytoskeletal composition of all compartments whose parent were not bifurcating. The bifurcation grid contained the

cytoskeletal composition of all bifurcation children. Depending on whether a compartment elongated or bifurcated, one (for elongations) or two (for bifurcations) pairs of microtubule and F-actin quantities were sampled and assigned to the newly added dendritic compartment(s). The sampling processes were constrained by microtubule and F-actin composition ordered by the weighted microtubule integral from the soma to the compartment's parent (see Methods for mathematical definition). The simulations ran until all compartments terminated (Fig. 4D) and the number of simulated neurons was matched to the number of real neurons for every cell group. Note that this generative model only describes arbor topology, branch length, and cytoskeletal distributions, but not the three-dimensional geometry of dendritic trees (bifurcation angles and branch meandering).

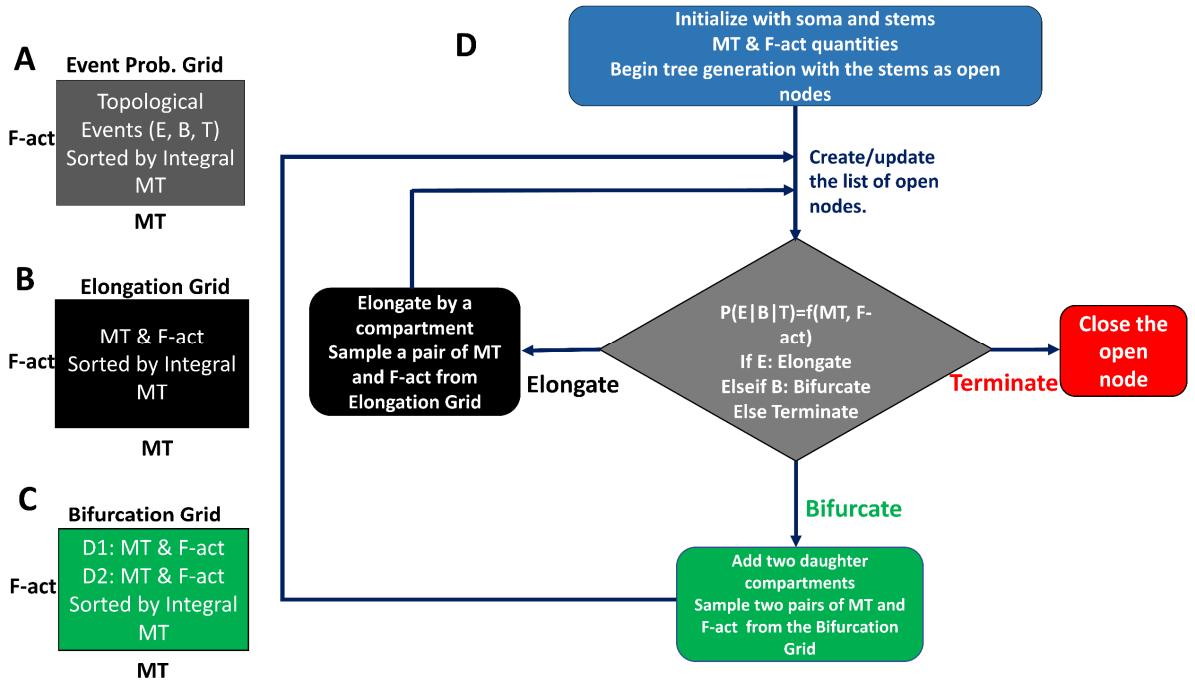

Fig. 4 Generative model description. Stochastic sampling is carried out from three data grids (A, B, C) binned by local microtubule (MT) and F-actin (F-act) quantities. The grids are used to sample (A) branch topology (elongation, bifurcation or termination), as well as the cytoskeletal compositions of the elongating (B) and bifurcating (C) compartments. All data are sampled from the bin that best matches the MT and F-act composition of the active compartment, with a bias for higher integral microtubule values (see Methods for definition). The tree generation process (D) starts with the initial MT and F-act concentration of the soma and the dendritic stem as active compartments. For each active compartment, branch topology sampling determines whether to elongate (adding one new compartment), bifurcate (adding two new compartments) or terminate (ending the branch). If a node elongates or bifurcates, the cytoskeletal composition of the newly created compartment(s) is sampled from the corresponding data grids. The process is repeated for all newly added nodes, until all branches terminate.

Simulated neurons fully reproduce morphology and cytoskeletal distributions across neuron groups

The dendrograms generated by the computational simulations were visually and qualitatively indistinguishable from those of the real neurons in size, complexity, and asymmetry for each of the three neuron groups (Fig. 5). Moreover, the simulated neurons of Class I, Class IV, and Class IV FormOE quantitatively reproduced all measured morphometric characteristics of their real counterparts, namely total dendritic length, number of terminal tips, topological and length asymmetry, and topological and length caulescence. Thus, relative to the model-generated Class I dendrograms, model-generated Class IV dendrograms were much longer and more complex, but had lower length and topological caulescence (SI Appendix, Table S1). The model-generated Class IV Form3OE dendrograms had generally intermediate values between the two WT subclasses in these measures. In all the quantified characteristics, the model fully reproduced the class-specific morphometrics in terms of group average and variance. None of the 18 two-tailed t-tests (6 measurements for each of 3 classes) comparing real and simulated neurons yielded significant differences ($p > 0.5$ even with no multiple testing correction).

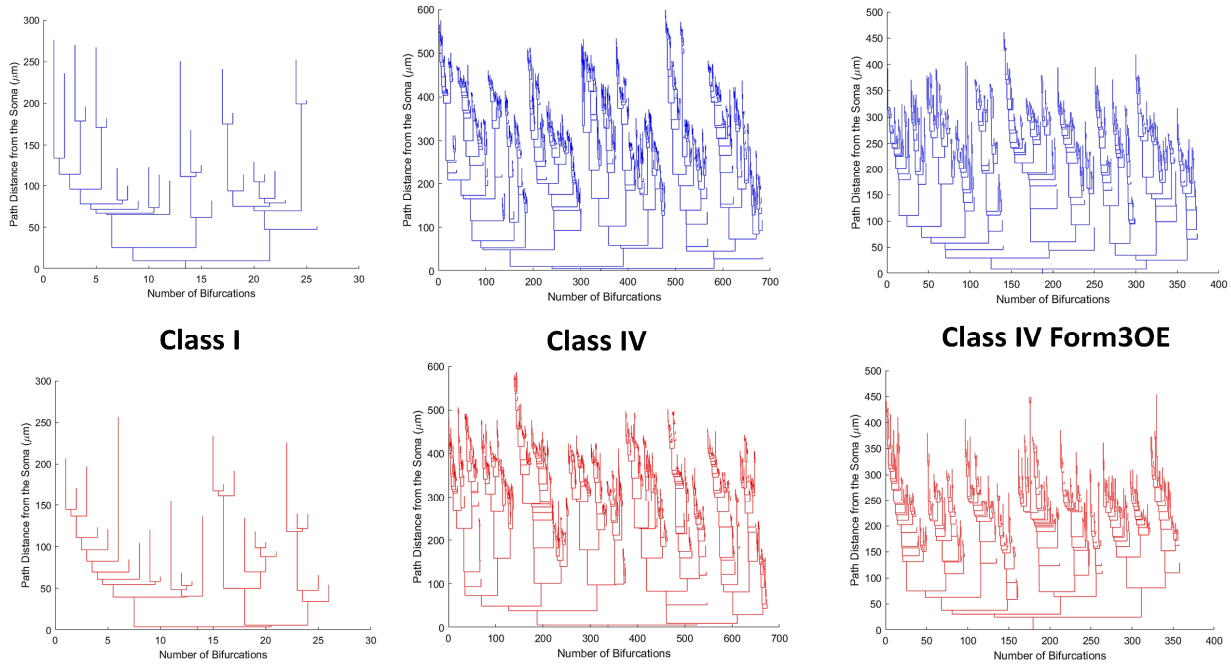

Fig. 5 Representative dendrograms of real (top, blue) and simulated (bottom, red) Class I (left), Class IV (middle), and mutant Class IV Form3OE (right) neurons.

Next, we compared real and simulated data by examining the distributions of dendritic length, microtubules, and F-actin as functions of path distance from soma and Strahler order. In all six cases the class-specific patterns of the simulated neurons were qualitatively and quantitatively almost identical to those of their real equivalents (Fig. 6). This showed that the model was not only able to capture the overall tree properties of Class I, Class IV, and Class IV Form3OE, but also their rise or decline across path distance and branch order.

Furthermore, simulated neurons exhibited similar relations between cytoskeletal composition and morphology as real neurons. Model-generated arbor length was highly correlated to local microtubule

quantity (SI Appendix, Table S2), but substantially less so in terminating branches (SI Appendix, Table S3), and F-actin enrichment was strongly associated with bifurcating compartments (SI Appendix, Fig. S4). Just as in real neurons, the correlation between microtubule and F-actin quantities also decreased with path distance in synthetic neurons (SI Appendix, Table S3). Finally, the computational model also reproduced the class-specific branch length (overall as well as separately for bifurcating and terminating branches) and the ratio between microtubule and F-actin quantities (SI Appendix, Table S4), thus replicating in the simulated neurons the parallel between the arbor size-to-complexity relation and the microtubule-to-F-actin relation observed in real cells.

Discussion

Microtubules and F-actin have long been implicated in neurostructural plasticity; however, their exact roles have not been fully elucidated due to the lack of their simultaneous quantification across the entirety of the neural arbor. With the use of the newly developed multi-signal reconstruction system (46), we quantified the arbor-wide microtubule and F-actin distributions from live images of fruit fly sensory neurons. Analysis of cytoskeletal distribution revealed the association of local microtubule with dendritic elongation (arbor size) and of local F-actin with dendritic branching (arbor complexity). These two distinct influences of microtubules and F-actin on dendritic morphology were consistent across structurally and functionally different cell types as well as a genetic alteration affecting cytoskeletal organization.

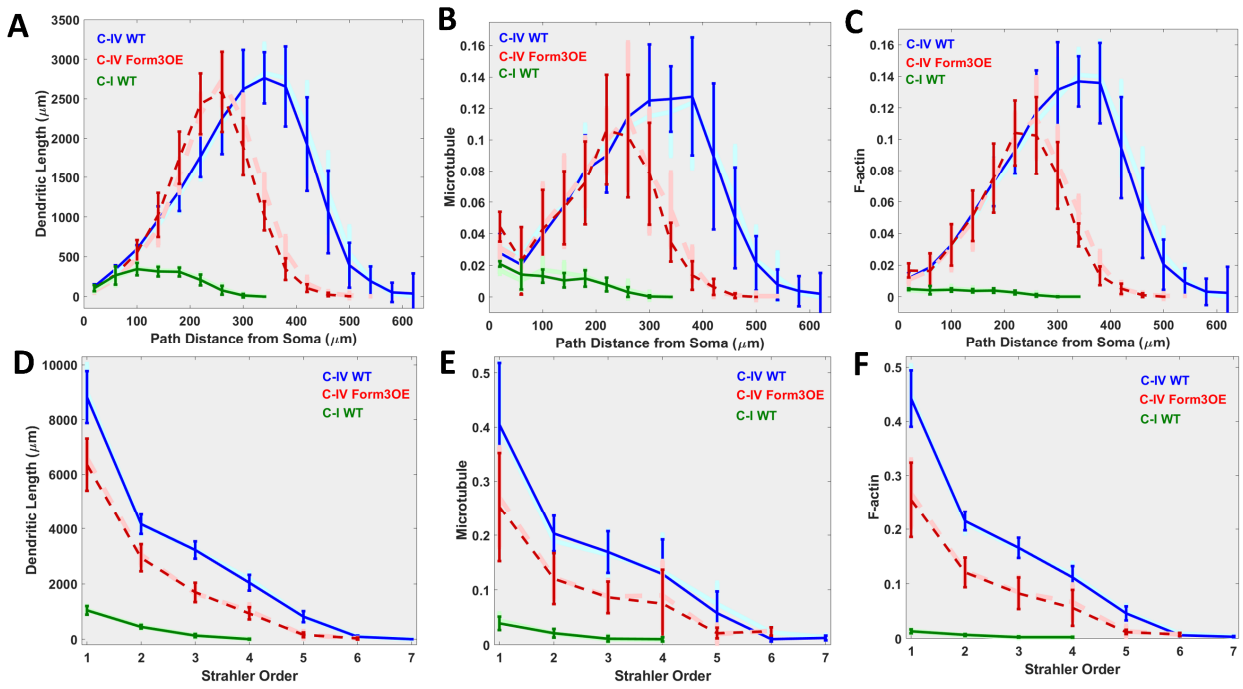

Fig. 6 Emergent distributions of dendritic length (A, D), microtubule (B, E) and F-actin (C, F) by path distance (A, B, C) and Strahler order (D, E, F) of simulated Class I (green), Class IV (blue) and Class IV Form3OE (red) neurons. Error bars indicate standard deviation. Corresponding distributions of real neurons are overlaid in lighter shades of blue, red and green.

The striking structural differences in dendritic morphology between WT Class I and Class IV da neurons is reflected in their substantially different functional roles and efferent patterns within the larval sensory system. Class I neurons participate in proprioceptive functions (55–58) whereas Class IV neurons are involved in polymodal nociception (59–61), chemosensation (62) and photoreception (63). Previous studies have also shown that genetic manipulations that alter overall morphology do not alter the size to complexity ratio of Class IV neurons. In contrast, Class I neurons drastically change their size to complexity ratio when genetically altered (14). Despite these structural and functional differentiations, the architectural rules revealed in this study remained consistent across the two da class extremes, quantitatively relating local cytoskeletal composition to the immediate branching behavior (bifurcation, elongation or termination) on the one hand, and to overall morphology (arbor length and asymmetry) on the other. In other words, the difference in arbor complexity and size between Class I and Class IV da neurons could be entirely explained by their different distribution patterns of microtubules and F-actin. Even genetic alterations in the mutant Class IV did not alter the fundamental relationships among local cytoskeletal composition, branching events, and overall arbor shape. The reduction in F-actin enrichment at branch points for Class IV Form3OE neurons relative to the WT was reflected in their relative reduction of overall branching complexity as well. We also observed across the three groups of neurons that the distribution patterns of microtubules were similar to those of F-actin in proximal, but not distal dendrites, which could be attributable to the transcription and transport of cytoskeletal monomers. Tubulin and actin monomers are produced at the soma, and then diffuse or get actively transported to the proximal branches first, followed by distal branches.

Almost all morphological characteristics analyzed in this study were statistically different between the three neuron groups. The proposed computational model, although simple, fully reproduced the group-by-group morphological and cytoskeletal properties observed in real neurons while demonstrating the correct relationships between cytoskeletal composition and arbor structure and vice versa. The morphological features captured by the model included total length and overall complexity, distribution of dendritic branches, asymmetry of length and branching, and prominence of main dendritic path. Cytoskeletal properties included arbor-wide distributions of microtubules and F-actin, correlation of microtubules with arbor length and association of branching with F-actin enrichment. Therefore, the analysis and modeling results jointly suggest that the diverse dendritic morphologies across all investigated cell groups shared similar underlying cytoskeletal mechanisms.

Consistent with the model, local increases in the quantity of stable microtubules through Formin3 overexpression further improved the correlation between microtubule quantity and arbor length. Increased F-actin signal by the same genetic alteration nearly doubled local F-actin quantity but actually reduced the enrichment levels at bifurcations. This suggests that enrichment events are more topology-specific in WT neurons, occurring when new branching events take place, while the tree-wide increase of F-actin in Form3OE decreases the difference between bifurcating and elongating compartments. As a combined result, Formin3 overexpression substantially lowered total dendritic length and arbor complexity in Class IV neurons, yielding a reduction in total F-actin and microtubule quantities despite the local increases of both cytoskeletal components. These observations corroborate the notion that Class IV neurons are evolutionarily optimized to fill a large amount of space through branching and elongation, maximizing the use of the available resources (47). Disrupting the distribution of the cytoskeletal resources could thus interfere with its space filling mechanisms (11, 48).

The consistent correlation observed between microtubule quantity and arbor length quantitatively confirms after forty years a seminal prediction based on early electron microscopy evidence (64): namely, that the number of microtubule polymers progressively decreases along the dendrites with distance from the soma and approaches zero near the terminal tips. Specifically, this decrease was posited to be gradual

within a branch, as some microtubules stop polymerizing, and discontinuous at bifurcations, where the microtubule polymers would partition between the two child dendrites. While the above conceptual model was originally formulated relying on sparse evidence from individual dendritic branches, our multi-signal dendritic reconstruction and analysis quantitatively corroborates it for the first time at the level of entire arbors and across neuron groups.

Those pioneering ideas along with initial ultrastructural observations that dendritic branch thickness closely corresponds with the number of microtubule polymers at that location (65) inspired a successful series of early computational simulations in which larger and smaller branch diameters increased the probability of bifurcating and terminating, respectively (53, 66). Another resource-driven phenomenological computer model posited the diffusion or active transport of somatically-produced tubulin to the neurite tips or growth cones where it would polymerize to extend the existing microtubule structure. The dynamic competition of tubulin among outgrowing branches can simulate simple as well as complex arbor morphologies (67). Other computational models finessed the influence of anterograde microtubule movement in tree generation by reducing the likelihood of generating new branches with path distance from soma or branch order (48, 50, 53, 68). The current study is unprecedented in driving the computational model directly by the experimentally recorded local cytoskeletal resources.

The enrichment of F-actin near dendritic bifurcations also constitutes a quantitative validation of recent experimental observations: actin blobs tend to stabilize at branch points, and nullifying that stabilization leads to a reduction in branch complexity (45). Another recent study has shown that Arp2/3 complex temporarily localizes at dendritic bifurcations to nucleate actin, leading to actin remodeling at the nascent branch point (31). Satellite Golgi outposts have also been observed at the dendritic branch points where microtubules are nucleated, and membrane proteins are produced (69). Higher F-actin levels may be important to maintain the presence of the Golgi apparatus at branch points since actin is involved in regulating Golgi structure and function (70). Interestingly, the differences in F-actin enrichment between terminating and elongating dendrites were much more modest. This may be because the reconstructions are from static image-stacks, providing a momentary snapshot of a structurally dynamic arbor. Hence, the compartments annotated as terminating could either be elongating or retracting. This idea is consistent with previous experimental observations that terminal branches remain dynamic even when the primary branches become stable (71).

Time-lapse imaging of dendritic morphology with multiple fluorescent proteins tagging the orientation of microtubule and F-actin polymerization will be informative for future studies to investigate further arbor plasticity and the underlying subcellular changes that drive it. We have recently developed an enhanced reconstruction system, where temporal changes in neuronal structure can be annotated simultaneously with subcellular changes (46). The time varying reconstructions with local polymerization information (rate and direction) may foster a deeper understanding of potential developmental mechanisms. The sufficiency of newly hypothesized rules of growth can then be tested by implementing a computational simulation constrained by the enhanced acquired data to verify whether it also reproduces dynamical phenomena like scaling, retraction and branch thickening. However, in order to become viable for use in developmental models, time-lapse reconstructions require the careful registration of image stacks, which is still exceedingly challenging at the level of entire dendritic arbors in vivo (72, 73).

Methods

Drosophila strains and live confocal imaging

Drosophila stocks were reared at 25˚C on standard cornmeal-molasses-agar media. Age-matched wandering third instar larvae of both sexes were used for all experiments. Fly strains used in this included: *w1118, UAS-GMA::GFP; GAL4[477],UAS-mCherry::Jupiter* (12) (CIV cytoskeletal reporter

strain); *w1118, UAS-GMA::GFP;+;GAL4[221],UAS-mCherry::Jupiter* (Class I cytoskeletal reporter strain); *UAS-form3-B1* (74). *w1118* was used as a genetic background control for outcrosses to the multi-fluorescent cytoskeletal transgene reports. We previously confirmed that expression of the F-actin and microtubule transgene reporters did not themselves exert any effects on dendritic development (12). Live confocal imaging was performed as previously described (12, 46, 48). Briefly, larvae were immersed in a 1:5 (v/v) diethyl ether to halocarbon oil on a cover slipped glass slide and neurons expressing fluorescent protein cytoskeletal reporter transgenes were visualized on a Zeiss LSM 780 confocal microscope. Images were collected as z-stacks at a step size of 1-2 microns and 1024 x 1024 resolution using a 20X air objective (Plan Apo M27, NA 0.8) and 1 airy unit for the pinhole. A total of 19 Class I ddaE, 10 Class IV ddaC, 9 mutant Class IV ddaC Form3OE neurons were imaged, reconstructed, analyzed and modeled. The digital morphological tracings and enhanced multi-signal ESWC files of all 38 neurons have been deposited to NeuroMorpho.Org (75) as part of the Ascoli and Cox archives. Images have been submitted to NeuroData.io.

Neuromorphometric analyses

Confocal images were semi-automatically reconstructed and edited in neuTube (76). Larval da neurons are relatively flat with limited dendritic arborization in the z dimension. Therefore, images containing high levels of noise (usually the top and bottom of the Z stacks) were removed and maximum intensity projection of the remaining stacks were used to guide the reconstructions process. The microtubule signal from the red channel and F-actin signal from the green channel were combined in FIJI (77) to create a third pseudo membrane channel from which the initial tracing was carried out. TREES Toolbox (78) was then used to resolve inaccuracies in tree topology and to resample the dendritic tree into compartment of uniform length (approximately 2 µm). These edited and resampled trees where then manually curated in neuTube once more and scaled from pixels to physical unit (µm) to generate the final SWC files. Multi-signal ESWC reconstructions (46) were produced in Vaa3D, using the Multichannel_Compute plugin, with the reconstructed SWC files and the multichannel images as input and a threshold of 10 for both channels (i.e. any intensity below 10 out of 255 was considered as 0). Specifically, the plugin was run twice, first with the basic SWC as the reconstruction and microtubule (RFP) as the secondary channel; and then a second time with the resultant multi-signal SWC from the first run as the reconstruction and F-actin (GFP) as the secondary channel. A combination of the red and green channels was used as the primary channel for both runs. The final multi-signal reconstructions contained sub-structural information for both microtubule and F-actin. The two signals were quantified in each compartment as the sum over all pixels in that compartment of the corresponding (MT or F-act) intensity divided by the maximum value of 255 to renormalize between 0 to 1 and reported per unit of length.

Custom scripts were written leveraging the TREES Toolbox (78) functions to calculate and plot multiple topological and cytoskeletal properties both locally and as arbor-wide distributions, including analysis of dendritic length and cytoskeletal protein expression vs. path distance from soma and Strahler (centripetal) order. Cytoskeletal quantities were normalized based on average total microtubule and average total F-actin of Class IV WT neurons.

Mathematical definitions of asymmetry and caulescence

Topological asymmetry (49) is defined as the average over all neuron bifurcations of the following function:

$$\boldsymbol{A_{td}} = \mathbf{0} \qquad \text{if } \boldsymbol{l_{td}} = \boldsymbol{r_{td}} = \mathbf{1}$$

$$\boldsymbol{A_{td}} = |\boldsymbol{l_{td}} - \boldsymbol{r_{td}}| \,/\, (\boldsymbol{l_{td}} + \boldsymbol{r_{td}} - \mathbf{2}) \quad \text{otherwise,}$$

where l_{td} and r_{td} represent the numbers of terminal tips (or terminal degree) respectively in the left the right subtrees of the bifurcation.

Length asymmetry is similarly defined as the average over all neuron bifurcations of the following function:

$$A_l = |l_l - r_l| / (l_l + r_l)$$

where ***l_l*** and ***r_l*** represent the arbor length respectively of the left the right subtrees of the bifurcation.

Topological caulescence (52) is the weighted topological asymmetry across the dendritic path from the soma to the terminal with the highest centrifugal branch order:

$$C_{td} = \sum |l_{td} - r_{td}| \ / \sum (l_{td} + r_{td})$$

Length caulescence is the weighted length asymmetry across the dendritic path from the soma to the terminal with the highest path distance from the soma:

$$C_l = \sum |l_l - r_l| \ / \sum (l_l + r_l)$$

Microtubule and F-actin based tree generation model

The data-driven model to simulate synthetic dendritic arbors was implemented in MATLAB (MathWorks, Natick, MA). This stochastic model uses three sampling grids: one for topological events and two for cytoskeletal composition (one each for elongating and bifurcating compartments). All three grids are two-dimensionally binned by local microtubule and F-actin quantities. The simulations started by sourcing the dendritic roots stemming from the soma of a real neuron as the 'open' compartments. Then, for every open compartment, the model identified the topological grid bin most closely matching the microtubule and F-actin quantities and sampled one of three topological events (elongation, bifurcation or termination) according to the following process. Data in the bin were first sorted by descending integral microtubule (***IM***), defined for $(i+1)^{th}$ compartment as:

$$IM_{i+1} = (IM_i * 0.99) + (MQ_i * 0.01)$$

where ***MQ*** is the microtubule quantity and the ith compartment is the parent of the $(i+1)^{th}$ compartment. Integral microtubule can equivalently be expressed as:

$$IM_{i+1} = 0.99 * MQ_0 + \sum_{j=1}^{i} (0.99)^{i-j} * MQ_j$$

where MQ_0 is the microtubule quantity at the root compartment. For sampling within a bin of n elements, first a number m was randomly chosen between 1 and n. This was followed by choosing a number between 1 and m and the process was repeated four additional times (totaling six iterations). The final number defined the sampled event in the sorted bin. Once an element was sampled, it was removed from the data bin.

If an elongation was sampled, a new compartment was added, sampling its cytoskeletal composition from the elongation grid with the same process described above. In case of bifurcations, two new compartments were added sampling their cytoskeletal compositions from the bifurcation grid. In case of termination, the compartment 'closed'. The simulations stopped when all compartment closed.

All analysis and modeling code have been deposited to ModelDB (senselab.med.yale.edu/modeldb).

Acknowledgements

The authors thank Mahan Mollajafar, Anna Lulushi, Akhil Goel and Alisha Compton for helping with neuron tracings.

References

1. Ledda F, Paratcha G (2017) Mechanisms regulating dendritic arbor patterning. *Cell Mol Life Sci* 74(24):4511–4537.
2. Franker M, Hoogenraad C (2013) Microtubule-based transport – basic mechanisms, traffic rules and role in neurological pathogenesis. *J Cell Sci* 126:2319–2329.
3. Lefebvre JL, Sanes Kay JR, J.N. (2015) Development of dendritic form and function. *Annu*.
4. Nanda S, Das R, Cox DN, Ascoli GA (2017) Structural Plasticity in Dendrites: Developmental Neurogenetics, Morphological Reconstructions, and Computational Modeling. *Neurobiological and Psychological Aspects of Brain Recovery*, ed Laura Petrosini (Springer Press, Contemporary 753 Clinical Neuroscience Series: Cham. 30), pp 1–34.
5. Jan Y-NN, Jan LYY (2010) Branching out: mechanisms of dendritic arborization. *Nat Rev Neurosci* 11(5):316–328.
6. Coles CH, Bradke F (2015) *Coordinating neuronal actin-microtubule dynamics* (Curr Biol 25: R677-R691) doi:10.1016/j.cub.2015.06.020.
7. Kapitein LC, et al. (2010) Mixed microtubules steer dynein-driven cargo transport in dendrites. *Curr Biol* 20(4):290–299.
8. Kapitein LC, Hoogenraad CC (2015) Building the Neuronal Microtubule Cytoskeleton. *Neuron* 87(3):492–506.
9. Santiago C, Bashaw GJ (2014) Transcription factors and effectors that regulate neuronal morphology. *Development* 141:4667–4680.
10. de la Torre-Ubieta L., Bonni A (2011) Transcriptional regulation of neuronal polarity and morphogenesis in the mammalian brain. *Neuron* 72:22–40.
11. Corty MM, Tam J, Grueber WB (2016) Dendritic diversification through transcription-factor mediated suppression of alternative morphologies. *Development* 143:1351–1362.
12. Das R, et al. (2017) Dendritic cytoskeletal architecture is modulated by combinatorial transcriptional regulation in Drosophila melanogaster. *Genetics* 207(4):1401–1421.
13. Iyer SC, Iyer EPR, Meduri R, Rubaharan M, Kuntimaddi A (2013) 2013a Cut, via CrebA, Transcriptionally Regulates the COPII Secretory Pathway to Direct Dendrite Development in Drosophila. *J Cell Sci* 126(20):4732–4745.

14. Iyer EPR, et al. (2013) Functional genomic analyses of two morphologically distinct classes of Drosophila sensory neurons: post-mitotic roles of transcription factors in dendritic patterning. *PLoS One* 8(8):72434.

15. Grueber WB, Jan LY, Jan YN (2003) Different levels of the homeodomain protein cut regulate distinct dendrite branching patterns of Drosophila multidendritic neurons. *Cell* 112(6):805–18.

16. Sugimura K, Satoh D, Estes P, Crews S, Uemura T (2004) Development of morphological diversity of dendrites in Drosophila by the BTB-Zinc finger protein Abrupt. *Neuron* 43(6):809–822.

17. Li W, Wang F, Menut L, Gao FB (2004) BTB/POZ-zinc finger protein abrupt suppresses dendritic branching in a neuronal subtype-specific and dosage-dependent manner. *Neuron* 43(6):823–834.

18. Ye B, et al. (2011) Differential regulation of dendritic and axonal development by the novel Krüppel-like factor Dar1. *J Neurosci* 31(9):3309–3319.

19. Jinushi-Nakao S, et al. (2007) Knot/Collier and cut control different aspects of dendrite cytoskeleton and synergize to define final arbor shape. *Neuron* 56(6):963–978.

20. Nagel JC, et al. (2012) Fascin controls neuronal class-specific dendrite arbor morphology. *Development* 139(16):2999–3009.

21. Iyer SC, et al. (2012) The RhoGEF trio functions in sculpting class specific dendrite morphogenesis in Drosophila sensory neurons. *PLoS One* 7(3):e33634.

22. Hattori Y, et al. (2013) Sensory-neuron subtype-specific transcriptional programs controlling dendrite morphogenesis: Genome-wide analysis of abrupt and knot/collier. *Dev Cell* 27(5):530–544.

23. Ferreira T, Ou Y, Li S, Giniger E, van Meyel DJ (2014) Dendrite architecture organized by transcriptional control of the F-actin nucleator Spire. *Development* 141(3):650–660.

24. Das R, et al. (2017) Formin3 regulates dendritic architecture via microtubule stabilization and is required for somatosensory nociceptive behavior. *bioRxiv*:227348.

25. Bray D, Bunge MB (1981) Serial analysis of microtubules in cultured rat sensory axons. *J Neurocytol* 10(4):589–605.

26. Howard J, Hyman AA (2009) Growth, fluctuation and switching at microtubule plus ends. *Nat Rev Mol Cell Biol* 10(8):569–574.

27. Alushin GM, et al. (2014) High-Resolution microtubule structures reveal the structural transitions in αβ-tubulin upon GTP hydrolysis. *Cell* 157(5):1117–1129.

28. Heidemann SR, Landers JM, Hamborg MA (1981) Polarity orientation of axonal microtubules. *J Cell Biol* 91(3):661–665.

29. Sánchez-Huertas C, et al. (2016) Non-centrosomal nucleation mediated by augmin organizes microtubules in post-mitotic neurons and controls axonal microtubule polarity. *Nat Commun* 7:12187.

30. Konietzny A, Bär J, Mikhaylova M (2017) Dendritic Actin Cytoskeleton: Structure, Functions, and Regulations. *Front Cell Neurosci* 11(May):1–10.

31. Stürner T, et al. (2019) Transient localization of the Arp2/3 complex initiates neuronal dendrite

branching in vivo. *Development* 146(7):pii: dev171397.

32. Smith BA, Daugherty-Clarke K, Goode BL, Gelles J (2013) Pathway of actin filament branch formation by Arp2/3 complex revealed by single-molecule imaging. *Proc Natl Acad Sci U S A* 110(4):1285–1290.

33. Chesarone MA, Dupage AG, Goode BL (2010) Unleashing formins to remodel the actin and microtubule cytoskeletons. *Nat Rev Mol Cell Biol* 11(1):62–74.

34. Breitsprecher D, Goode BL (2013) Formins at a glance. *J Cell Sci* 126(1):1–7.

35. Thurston SF, Kulacz WA, Shaikh S, Lee JM, Copeland JW (2012) The ability to induce microtubule acetylation is a general feature of Formin proteins. *PLoS One* 7(10):e48041.

36. Flynn KC, et al. (2012) ADF/Cofilin-Mediated Actin Retrograde Flow Directs Neurite Formation in the Developing Brain. *Neuron* 76(6):1091–107.

37. Unsain N, Stefani FD, Cáceres A (2018) The actin/spectrin membrane-associated periodic skeleton in neurons. *Front Synaptic Neurosci* 10:10.

38. Georges PC, Hadzimichalis NM, Sweet ES, Firestein BL (2008) The yin-yang of dendrite morphology: Unity of actin and microtubules. *Mol Neurobiol* 38(3):270–284.

39. Yalgin C, et al. (2015) Centrosomin represses dendrite branching by orienting microtubule nucleation. *Nat Neurosci* 18(10):1437–1445.

40. Portran D, et al. (2017) Tubulin acetylation protects long-lived microtubules against mechanical ageing. *Nat Cell Biol* 19(4):391–398.

41. Feng C, et al. (2019) Patronin-mediated minus end growth is required for dendritic microtubule polarity. *J Cell Biol* 218(7):2309–2328.

42. Chia JX, Efimova N, Svitkina TM (2016) Neurite outgrowth is driven by actin polymerization even in the presence of actin polymerization inhibitors. *Mol Biol Cell* 27(23):3695–3704.

43. Mortal S, et al. (2017) Actin Waves Do Not Boost Neurite Outgrowth in the Early Stages of Neuron Maturation. *Front Cell Neurosci* 11:402.

44. Sundararajan L, et al. (2019) Actin assembly and non-muscle myosin activity drive dendrite retraction in an UNC-6/Netrin dependent self-avoidance response. *PLOS Genet* 15(6):e1008228.

45. Nithianandam V, Chien CT (2018) Actin blobs prefigure dendrite branching sites. *J Cell Biol* 217(10):3731–3746.

46. Nanda S, et al. (2018) Design and implementation of multi-signal and time-varying neural reconstructions. *Sci Data* 5:1–10.

47. Grueber WB, Jan LY, Jan YN (2002) Tiling of the Drosophila epidermis by multidendritic sensory neurons. *Development* 129:2867–2878.

48. Nanda S, Das R, Bhattacharjee S, Cox DN, Ascoli GA (2018) Morphological determinants of dendritic arborization neurons in Drosophila larva. *Brain Struct Funct* 223(3):1107–1120.

49. Van Pelt J, et al. (1992) Tree asymmetry-A sensitive and practical measure for binary topological trees. *Bull Math Biol* 54(5):759–784.

50. Samsonovich A V., Ascoli GA, V. SA, GA A (2005) Statistical determinants of dendritic morphology in hippocampal pyramidal neurons: A hidden Markov model. *Hippocampus* 15(2):166–183.

51. Brown KM, Gillette TA, Ascoli GA (2008) Quantifying neuronal size: Summing up trees and splitting the branch difference. *Semin Cell Dev Biol* 19(6):485–493.

52. Burke RE, Marks WB, Ulfhake B (1992) A parsimonious description of motoneuron dendritic morphology using computer simulation. *J Neurosci* 12(6):2403–2416.

53. Donohue DE, Ascoli GA (2008) A Comparative Computer Simulation of Dendritic Morphology. *PLoS Comput Biol* 4(6):e1000089.

54. Ascoli GA, Krichmar JL, Scorcioni R, Nasuto SJ, Senft SL (2001) Computer generation and quantitative morphometric analysis of virtual neurons. Anat Embryol. *Anat Embryol (Berl)* 204(4):283–301.

55. Hughes CL, Thomas JB (2007) A sensory feedback circuit coordinates muscle activity in Drosophila. *Mol Cell Neurosci* 35(2):383–396.

56. Cheng LE, Song W, Looger LL, Jan LY, Jan YN (2010) The role of the TRP channel NompC in Drosophila larval and adult locomotion. *Neuron* 67:373–380.

57. He L, et al. (2019) Direction Selectivity in Drosophila Proprioceptors Requires the Mechanosensory Channel Tmc. *Curr Biol* 29(6):945–956.

58. Vaadia RD, et al. (2019) Characterization of proprioceptive system dynamics in behaving Drosophila larvae using high-speed volumetric microscopy. *Curr Biol* 29(6):935–944.

59. Tracey WD, Wilson RI, Laurent G, Benzer S (2003) painless, a Drosophila gene essential for nociception. *Cell* 113:261–273.

60. Hwang RY, et al. (2007) Nociceptive neurons protect Drosophila larvae from parasitoid wasps. *Curr Biol* 17(24):2105–2116.

61. Lopez-Bellido R, Himmel NJ, Gutstein HB, Cox DN, Galko MJ (2019) An assay for chemical nociception in Drosophila larvae. *Phil Trans R Soc B* 374:20190282.

62. Himmel NJ, et al. (2019) Drosophila menthol sensitivity and the Precambrian origins of transient receptor potential-dependent chemosensation. *Phil Trans R Soc B* 374:20190369.

63. Xiang Y, et al. (2010) Light-avoidance-mediating photoreceptors tile the Drosophila larval body wall. *Nature* 468(7326):921–926.

64. Hillman D (1979) Neuronal shape parameters and substructures as a basis of neuronal form. *The Neurosciences, Fourth Study Program*, ed Schmitt FO WF (Cambridge, MA), pp 477–498.

65. Hillman DE, Llinás R, Chujo M, Crank R (1980) *Direct analysis of nervous system ultrastructure by computer control of STEM.* (Pt).

66. Schneider CJ, Bezaire M, Soltesz I (2012) Toward a full-scale computational model of the rat dentate gyrus. *Front Neural Circuits* 6(NOV):1–8.

67. Hjorth JJJJ, Van Pelt J, Mansvelder HD, Van Ooyen A (2014) Competitive dynamics during resource-driven neurite outgrowth. *PLoS One* 9(2):e86741.

68. Van Pelt J, Uylings HBM, J VP, H U (2002) Branching rates and growth functions in the outgrowth of dendritic branching patterns. *Network-Comp Neural* 13(3):261–281.

69. Ori-McKenney KM, Jan LY, Jan YN (2012) Golgi outposts shape dendrite morphology by functioning as sites of acentrosomal microtubule nucleation in neurons. *Neuron* 76(5):921–930.

70. Gu F, Crump CM, Thomas G (2001) Trans-Golgi network sorting. *Cell Mol Life Sci* 58(8):1067–1084.

71. Lee SB, Bagley JA, Lee HY, Jan LY, Jan Y-N (2011) Pathogenic polyglutamine proteins cause dendrite defects associated with specific actin cytoskeletal alterations in Drosophila. *Proc Natl Acad Sci* 108(40):16795–16800.

72. Rada L, et al. (2018) Tracking-assisted Detection of Dendritic Spines in Time-Lapse Microscopic Images. *Neuroscience* 394:189–205.

73. Sheintuch L, et al. (2017) Tracking the Same Neurons across Multiple Days in Ca2+ Imaging Data. *Cell Rep* 21(4):1102–1115.

74. Tanaka H, et al. (2004) Formin3 is required for assembly of the F-actin structure that mediates tracheal fusion in Drosophila. *Dev Biol* 274(2):413–425.

75. Ascoli GA, Donohue DE, Halavi M (2007) NeuroMorpho.Org: A central resource for neuronal morphologies. *J Neurosci* 27(35):9247–9251.

76. Feng L, Zhao T, Kim J (2015) *neuTube 1.0: A new design for efficient neuron reconstruction software based on the SWC Format* (eNeuro 2) doi:10.1523/ENEURO.0049-14.2014.

77. Schindelin J, et al. (2012) Fiji: an open-source platform for biological-image analysis. *Nat Methods* 9(7):676–682.

78. Cuntz H, Forstner F, Borst A, Ha M, Häusser M (2010) One rule to grow them all: a general theory of neuronal branching and its practical application. *PLoS Comput Biol* 6(8):1000877.